Journal of Electrochemistry

Volume 30 | Issue 9

2024-08-28

Optimization of Channel Structure of Alkaline Water Electrolyzer by Using Expanded Mesh as Bipolar Plate

Hai-Yan Xiong

Zhen-Xiao Zhu

Xin Gao

Chen-Ming Fan

Hui-Bao Luan
Shanghai Marine Diesel Engine Research Institute Shanghai 201108, China, luanhuibao@163.com

Bing Li
School of Mechanical and Power Engineering East China University of Science and Technology, Shanghai 200237, China, bingli@ecust.edu.cn

Recommended Citation

Hai-Yan Xiong, Zhen-Xiao Zhu, Xin Gao, Chen-Ming Fan, Hui-Bao Luan, Bing Li. Optimization of Channel Structure of Alkaline Water Electrolyzer by Using Expanded Mesh as Bipolar Plate[J]. *Journal of Electrochemistry*, 2024 , 30(9): 2312281.
DOI: 10.61558/2993-074X.3469
Available at: https://jelectrochem.xmu.edu.cn/journal/vol30/iss9/9

ARTICLE

Optimization of Channel Structure of Alkaline Water Electrolyzer by Using an Expanded Mesh as a Bipolar Plate

Hai-Yan Xiong [a], Zhen-Xiao Zhu [a], Xin Gao [a], Chen-Ming Fan [a], Hui-Bao Luan [b,*], Bing Li [a,*]

[a] School of Mechanical and Power Engineering East China University of Science and Technology, Shanghai 200237, China
[b] Shanghai Marine Diesel Engine Research Institute Shanghai 201108, China

Abstract

Alkaline water electrolysis (AWE) is the most mature technology for hydrogen production by water electrolysis. Alkaline water electrolyzer consists of multiple electrolysis cells, and a single cell consists of a diaphragm, electrodes, bipolar plates and end plates, etc. The existing industrial bipolar plate channel is concave-convex structure, which is manufactured by complicated and high-cost mold punching. This structure still results in uneven electrolyte flow and low current density in the electrolytic cell, further increasing in energy consumption and cost of AWE. Thereby, in this article, the electrochemical and flow model is firstly constructed, based on the existing industrial concave and convex flow channel structure of bipolar plate, to study the current density, electrolyte flow and bubble distribution in the electrolysis cell. The reliability of the model was verified by comparison with experimental data in literature. Among which, the electrochemical current density affects the bubble yield, on the other hand, the generated bubbles cover the electrode surface, affecting the active specific surface area and ohmic resistance, which in turn affects the electrochemical reaction. The result indicates that the flow velocity near the bottom of the concave ball approaches zero, while the flow velocity on the convex ball surface is significantly higher. Additionally, vortices are observed within the flow channel structure, leading to an uneven distribution of electrolyte. Next, modelling is used to optimize the bipolar plate structure of AWE by simulating the electrochemistry and fluid flow performances of four kinds of structures, namely, concave and convex, rhombus, wedge and expanded mesh, in the bipolar plate of alkaline water electrolyzer. The results show that the expanded mesh channel structure has the largest current density of 3330 A/m^2 and electrolyte flow velocity of 0.507 m/s in the electrolytic cell. Under the same current density, the electrolytic cell with the expanded mesh runner structure has the smallest potential and energy consumption. This work provides a useful guide for the comprehensive understanding and optimization of channel structures, and a theoretical basis for the design of large-scale electrolyzer.

Keywords: Alkaline water electrolyzer; Expanded mesh channel structure; Numerical simulation

1. Introduction

Traditional fossil fuels not only have limited reserves, but also caused high carbon emissions and serious greenhouse effect. In recent years, renewable clean energy, including solar energy, wind energy, etc., has been booming in the world to replace traditional fossil fuels and achieve energy transformation [1–5]. Hydrogen energy, a clean secondary energy of high thermal value, as energy carriers and raw materials, widely used in renewable energy integration, metallurgy, synthetic ammonia, and hydrogen-synthetic fuel, etc [6–10]. Among various hydrogen production methods, electrolytic water hydrogen is the cleanest hydrogen production technology, and currently

Received 28 December 2023; Received in revised form 17 April 2024; Accepted 7 May 2024
Available online 15 May 2024

* Corresponding author, Hui-Bao Luan, E-mail address: luanhuibao@163.com.
* Corresponding author, Bing Li, E-mail address: bingli@ecust.edu.cn.

https://doi.org/10.61558/2993-074X.3469

accounts for only about 5%, but it is predicted that it has high potential market value [11−16].

Electrolytic water hydrogen production [17−22] is divided into: alkaline water electrolysis (AWE) [23−26], proton exchange membrane electrolysis (PEM) [27,28], solid oxide electrolysis (SOE) and anion exchange membrane electrolysis (AEM). Among them, AWE is currently the most mature and lowest cost electrolytic hydrogen production technology with a single cell scale of 3000 Nm^3/h, and has achieved a large-scale industrialized hydrogen production [19]. However, the cost of the AWE is still far higher than that of the conventional hydrogen production technology, such as reforming fossil fuels (coals, natural gas, etc.). Therefore, it is urgent to further lower the cost and increase market competition of AWE.

Cost reduction can be achieved by reducing the cost of electrolyzer equipment and improving the efficiency of the electrolyzer. Alkaline water electrolyzer is mainly composed of electrodes, diaphragm, bipolar plates and end plates, etc. Traditionally, the bipolar plate of AWE has concave-convex structure that is complicated and difficult to be fabricated by mold punching with high manufacturing costs. Besides, AWE has lower current density and high energy consumption problems. Currently industrial concave-convex bipolar plates exist the problem of uneven electrolyte flow. The uneven flow of electrolyte hinders the ion and heat transfers on the electrode surface, and the bubbles without escape in time accumulate on the electrode, reducing the active specific surface area of the electrode and increasing the activation overpotentials and ohmic drop, thus increasing the energy consumption and cost of AWE [19,29,30]. Therefore, it is necessary to improve the uniformity of the electrolyte distribution and accelerate the bubble escape by optimizing the bipolar plate channel structure [30−35].

Modeling is an essential tool for the rapid development of AWE, which is beneficial to channel structure, process parameters optimization and large-scale electrolyzer analysis [18,36−38]. AWE modeling researches have been firstly focused on the 2D physical field analysis, such as thermodynamics, flow, heat transfer, without involving in flow field structure and experimental verification. For example, Hammoudi et al. [37] proposed a 2D multi-physical model describing the evolution of the operating voltage of an electrolysis based on electrochemistry, thermodynamics and two-phase flow. Olivier et al. [36] reviewed the 2D electrochemical and heat transfer (lumped heat capacity method) models of AWE electrolysis, without considering the flow field structure and mass transfer model of AWE. Hu et al. [39] made a detailed and comprehensive review of the existing modeling work on 2D AWE thermodynamics, electrochemistry, heat and gas purity.

Recently, Huang et al. [38] established a 3D traditionally integrated channel structure model, considering the bubble effect, the coupling equation of electrochemical and mixture model for the two-phase laminar flow. The results show that when the current density is higher than 2500 A/m^2, the relative error of the model's current-voltage (I-V) characteristic curve is less than 5%. Further, Zhang et al. [40] modeled and simulated the spherical concave and convex (SCC) Euler-Euler RANS k-ε turbulence model, proving that the SCC-shaped bipolar plate structure could effectively average the distributions of electrolyte and bubbles in the channel, and reduced the hydrogen gas concentration on the electrode surface by comparing with the straight channel, which was conducive to the improvement of electrolytic efficiency. Besides, Wang et al. [41] also established a 3D laminar model to study the uniformity of liquid flow in the concave-convex bipolar plate (CCBP) electrolyzer, and combined with visual experiments to verify the simulation results, revealing the obvious non-uniform flow in the CCBP electrolyzer. Subsequently, Wang et al. [42] compared the flow uniformity of blank, CCBP, wedge, and rhombus electrolyzers, by using a laminar flow model, with that of conventional CCBP electrolyzer, and found that the flow uniformity values of wedge and CCBP electrolyzers were, respectively, increased by 19% and 28%. Zhao et al. [43,44] designed an industrial system-level AWE hydrogen production equipment, comparing the concave-convex structure and expanded mesh structure as a bipolar plate by experiments. There are some literatures concerning simulation models of 3D alkaline water electrolyzer channel structures, but very few study deals with expanded mesh channel structures, and especially, until now the researches about a comprehensive analysis of the electrochemical and flow performances within the electrolytic cells of expanded mesh channel structures have not yet been reported from the perspective of theoretical studies.

In this work, we firstly establish an electrochemical and RNG κ-ε phase transfer mixture model based on the industrial concave-convex bipolar plate channel structure. The model is verified with the experimental values in the literature, which ensures the accuracy and reduces the calculation cost. Secondly, the simulation and comparison of bipolar plate electrolytic cell with concave-convex, rhombus, wedge and expanded

mesh structures were carried out to study the optimal bipolar plate channel structure, analyze its internal electrochemistry and flow field distribution, and achieve the goal of reducing energy consumption and cost of AWE.

2. Methodology

2.1. Geometric modelling

The large alkaline water electrolyzer consists of multiple electrolytic cells, in which the structure is identical of each electrolytic cell, making this article firstly focuses on a single electrolytic cell. Zero-gap electrolytic cell structure is adopted to reduce the internal resistance of electrolyte and improve the electrolysis efficiency by reducing the distance between electrodes and diaphragm. As shown in Fig. 1, the geometrical model of a zero-gap alkaline water electrolytic cell consists of a cathode, an anode, and a diaphragm, as well as cathodic and anodic flow channels field (the flow channel between the bipolar plate and the electrode), through which we focus on the effect of the bipolar plate structure. Wherein, the 3D porous electrode and diaphragm domains are assumed to be homogeneous cylindrical domains having porosities of 0.27 and 0.56, respectively [45].

Figure 2(a−d) shows the geometrical models of the concave-convex, rhombus, wedge and expanded mesh flow field structures on the bipolar plate. The single unit of the rhombus structure is a square with a height of 2 mm; the single unit of the rhombus structure is a rhombus formed by the stacking of two rectangles, with the length of the rectangles 2.5 mm, half the width of the length and the height of the rhombuses 2.5 mm; and the expanded mesh structure consists of a staggered structure with a long intercept of 12 mm, a short intercept of about 8.5 mm, and a total thickness of 2.33 mm, the model parameters are shown in Table 1.

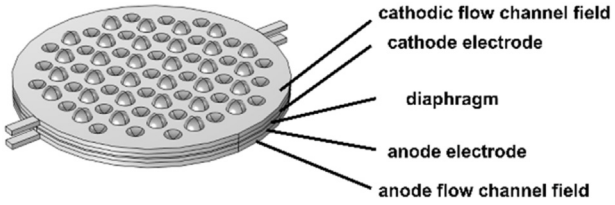

Fig. 1. A semantical representation of a filter-press type alkaline water electrolysis cell.

3. Mathematical models of the electrolyzer cell

3.1. Electrochemical model

Alkaline water electrolysis overall reactions:

$$\text{Cathode reaction}: 2H_2O\text{-}2e^- \rightarrow 2OH^- + H_2 \quad (1)$$

Table 1. Four types of bipolar plate flow field structure dimensions.

	Geometric parameter	Value (mm)
	Electrode radius	65
	Electrode height	2
	Diaphragm radius	65
	Diaphragm height	0.7
	Inlet length	6
	Inlet width	6
	Channel radius	65
	Channel height	2
Single unit		
Concave-convex structure	Concave/convex sphere radius	4.5
	Concave and convex spheres distance	12
Rhombus	Height	2
	Channel height	3
Wedge	Length	2.5
	Width	1.25
	Height	2.5
	Channel height	3
Expanded mesh	Thickness	0.5
	Height	2.33
	Transverse distance	6
	Longitudinal distance	4.23

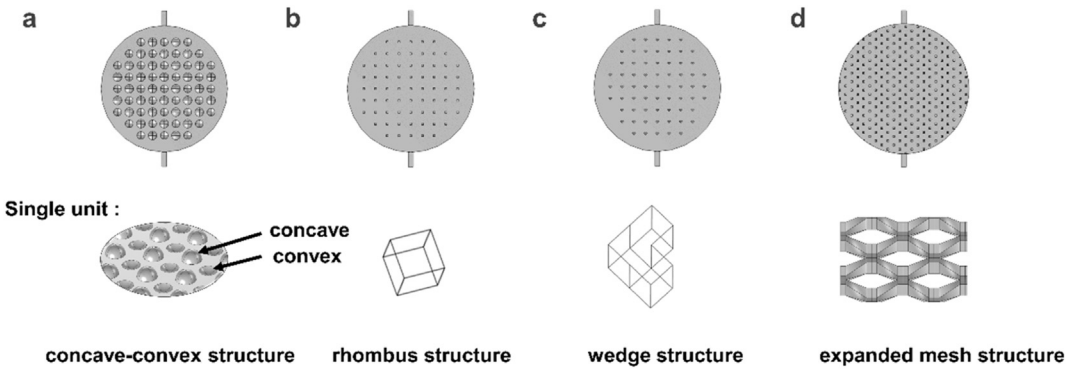

Fig. 2. (a) The concave-convex structure flow path, (b) rhombus structure flow path, (c) wedge structure flow path and (d) expanded mesh structure flow path.

$$\text{Anode reaction}: 4OH^{-}\text{-}4e^{-} \rightarrow 2H_2O + O_2 \quad (2)$$

There are mainly three kinds of overpotential in a single cell:

(1) Activation overpotential;
(2) Ohmic overpotential;
(3) Diffusion overpotential;

Alkaline water electrolytic cell has ignored concentration overpotential due to low current densities and high OH^{-} concentrations [46,47]. Thereby, only the activation overpotential and ohmic overpotential are considered, and the equations are as follows:

$$E_{\text{cell}} = E_{\text{rev}} + E_{\text{act,ano}} + E_{\text{act,cat}} + E_{\text{ohm}} \quad (3)$$

Where E_{rev} is the reversible voltage of a single cell, $E_{\text{act,ano}}$ and $E_{\text{act,cat}}$ are the activation overpotentials of the anode and cathode, respectively, E_{ohm} is the ohmic overpotential.

According the Nernst equation [48]:

$$E_{\text{rev}} = E^{0}_{\text{rev}} + \frac{R*T}{2*F}\ln\frac{P_{H_2}\sqrt{P_{O_2}}}{P_{H_2O}} \quad (4)$$

P_{H_2}, P_{O_2} and P_{H_2O} are the partial pressures of H_2, O_2 and H_2O.

Assuming that the concentration of each substance is the same everywhere, $C_{PE} = C_{PS}$, $C_{RE} = C_{RS}$, the activation overpotential-current relationship follows the Butler-Volmer equation [48]:

$$i_{loc} = i_0\left[e^{\left(\frac{\alpha_a*F*\eta}{R*T}\right)} - e^{\left(\frac{-\alpha_c*F*\eta}{R*T}\right)}\right] \quad (5)$$

where i_{loc} means the current density at the electrode, i_0 is the exchange current density, α_a , α_c are the electrode electron transfer factors, F is the Faraday's constant, $F = 96485.33$ C/mol, R is the molar gas constant, and T is the temperature.

For both cathodic and anodic electrode reactions, when either cathodic or anodic polarization dominates, the overpotentials conform to the Tafel equation as shown in (6−7) [48]:

$$E_{act,a} = \frac{RT}{n*\alpha_a*F}*ln\frac{i_{loc}}{i_{0,a}} \quad (6)$$

$$E_{act,c} = \frac{RT}{n*\alpha_c*F}*\ln\frac{i_{loc}}{i_{0,c}} \quad (7)$$

The active specific surface area is determined by considering a reduction in the active area for electrochemical reactions due to bubble coverage:

$$a_v = S*(1-\theta) \quad (8)$$

a_v is the electrode reaction area, S is the specific surface area of the electrocatalyst, calculated by surface area/volume in m^2/m^3, i.e. $1/m$, θ is the bubble volume fraction, calculated by flow modelling.

$$i_v = a_v*i_{loc} \quad (9)$$

The ohmic overpotential is the loss caused by the resistances of the electrodes, electrolyte and diaphragm. The total ohmic overpotential consists of the electrolyte, electrode and diaphragm overpotentials and is expressed as follows:

$$E_{\text{ohm}} = I*\left(R_a + R_c + R_{l_{bubble}} + R_{mem}\right) \quad (10)$$

Where R_{a} and R_{c} represent the anode and cathode electrode resistances, respectively, $R_{\text{l}_{\text{bubble}}}$ represents the electrolyte resistance considering the effect of bubbles, and R_{mem} means the diaphragm resistance, while the conductivity σ_{mem} is set to be 20.44 S/m [45]. The related calculations are given below:

$$R = \frac{1}{\sigma}*\left(\frac{L}{S}\right) \quad (11)$$

$$\begin{aligned}\sigma_a = \sigma_c = \sigma_{Ni} &= 60000000 - 279650*T + 532*T^2 \\ &\quad - 0.38057*T^3\end{aligned} \quad (12)$$

$$\begin{aligned}\sigma_{KOH} = {} & 2.041*m_{KOH} - 0.0028*{m_{KOH}}^2 \\ & + 0.005332*m_{KOH}*T + 207.2*\frac{m_{KOH}}{T} \\ & + 0.001043*{m_{KOH}}^3 - 0.0000003*{m_{KOH}}^2*T^2\end{aligned} \quad (13)$$

$$\begin{aligned}m_{KOH} = m_{wt}*\Big(& 183.1221 - 0.56845*T \\ & + 984.5679*e^{\left(\frac{m_{wt}}{115.96277*5610.5}\right)}\Big)\end{aligned} \quad (14)$$

Where m_{wt} represents the mass fraction of alkaline water electrolysis electrolyte, and the industrial alkaline mass fraction is 30%. The effective conductivity of the electrolyte is corrected according to the Bruggeman equation:

$$\sigma_{l,eff} = {\varepsilon_l}^{1.5}*\sigma_l \quad (15)$$

where ε_l is the effective volume fraction of the electrolyte, and the electrode substrate is a 60-mesh Ni mesh with a porosity of 0.2695, i.e., $\varepsilon_l = 0.2695$ [45], taking the effect of bubbles into account:

$$\sigma_{l_{bubble}} = \sigma_{l,eff}*(1-\theta) \quad (16)$$

There is a difference between the current conservation equation and the potential equation

at the electrode-electrolyte interface due to the presence of an overpotential, as shown in Eqs. 17 and 18:

$$i_l = -\sigma_{l,eff} * \nabla \Phi_l \ \nabla i_l = i_v \tag{17}$$

$$i_s = -\sigma_s * \nabla \Phi_s \ \nabla i_s = -i_v \tag{18}$$

where i_s (A/m^2) and i_l (A/m^2) denote the current density vectors, Φ (V) represents the potentials in the metal conductor and electrolyte, while the subscripts s and l represent the electrodes and electrolyte, respectively.

3.2. RNG κ-ε phase transfer mixture model

This article focuses on the uniformity of the electrolyte flow, which is the basis of the overall gas-liquid flow uniformity during the electrolysis process; therefore, the electrolyte flow in an alkaline water electrolyzer can be calculated by solving the single-phase steady-state continuity equations and the Navier-Stokes equations. Water vapor and H_2/O_2 gas crossover are not considered, and the volume change that exists is between liquid water and H_2/O_2 gas, and the sum of the volume fractions of the two phases within each computational mesh is 1. Secondly, according to previous studies, the flow in alkaline water electrolyzer is of dispersive turbulence [49,50]. Therefore, the phase transfer mixture model is established, which is a relatively simplified dispersion-type flow model that requires only a set of mass and momentum equations to be calculated. In addition, the RNG κ-ε model improves the model convergence by attaching a turbulent dissipation term ε to the equations. Eventually, the RNG κ-ε phase transfer mixture model is considered and selected in this study to simulate the flow characteristics inside the alkaline water electrolyzer, which can lead to the following equations:

Mass conservation equation (continuity equation):

$$\nabla * (\rho \vec{u}) = 0 \tag{19}$$

Momentum conservation equation:

$$\rho(\vec{u} * \nabla)\vec{u} = \nabla * \left[-p\vec{I} + \vec{K}\right] + \vec{F} + \rho g \tag{20}$$

The turbulent flow is modeled using the κ-ε model to solve for the turbulent kinetic energy κ and turbulent dissipation ε, which are calculated as follows:

$$\rho \frac{\partial \kappa}{\partial t} + \rho(\vec{u} * \nabla)\kappa = \nabla * \left[\left(\mu + \frac{\mu_T}{\sigma_k}\right)\nabla \kappa\right] + P_k - \rho\varepsilon \tag{21}$$

$$\rho \frac{\partial \varepsilon}{\partial t} + \rho(\vec{u} * \nabla)\varepsilon = \nabla * \left[\left(\mu + \frac{\mu_T}{\sigma_\varepsilon}\right)\nabla \varepsilon\right] + C_{\varepsilon 1}\frac{\varepsilon}{k}P_k - C_{\varepsilon 2}\rho\frac{\varepsilon^2}{k} \tag{22}$$

$$\frac{3C_{d,i}\rho_c}{4d_i}u_{slip,i}\overrightarrow{u_{slip,i}} = -(\rho - \rho_{s_i})\left(\frac{\partial \overrightarrow{u_m}}{\partial t} - \overrightarrow{u_m} * \nabla \overrightarrow{u_m} + g + \frac{F}{\rho}\right) \tag{23}$$

Where ρ is the density of the mixture, ρ_{s_i} is the density of the bubble phase, u is the velocity vector of the mixture, P is the fluid pressure, μ is the mixture viscosity, μ_T is the turbulent viscosity, F is the external force, g is the acceleration of gravity, u_{slip} is the slip velocity, $C_{d,i} = 0.44$; the empirical coefficients $C_{\varepsilon 1} = 1.42$ and $C_{\varepsilon 2} = 1.68$.

The mass sources of H_2 and O_2 are calculated by Faraday's law as following [51]:

$$m_{H_2} = \frac{i_v * M_{H_2}}{2 * F} \tag{24}$$

$$m_{O_2} = \frac{i_v * M_{O_2}}{4 * F} \tag{25}$$

Where i_v (A/m^3) means the volume current density, M_{H_2}, and M_{O_2} (g/mol) mean the relative molecular masses of H_2 and O_2, respectively.

Mass transfer between liquid water and gas phases in the electrode domain:

$$\nabla N_i = qs_{si} \tag{26}$$

$$m_{liquid} = \pm\frac{i_v * M_{OH}}{F} \tag{27}$$

qs_{si} (kg/m^3·s) means the mass transfer to other terms, where qs_{si} is equal to m_{liquid}, which means the electrolyte transport through the diaphragm due to electrochemical reactions, positive on the hydrogen electrode domain and negative on the oxygen electrode domain; qs_{si} is equal to m_{H_2} on the H_2 electrode domain and m_{O_2} on the O_2 electrode domain.

The electrochemical current density affects the bubble yield, on the other hand, the generated bubbles cover the electrode surface, affecting the active specific surface area, which in turn affects the electrochemical reaction, achieving a bidirectional coupling between electrochemistry and flow, as showing in Fig. 3.

3.3. Boundary conditions

The hydrogen side of the electron-conducting phase is set to be electrically grounded, and the

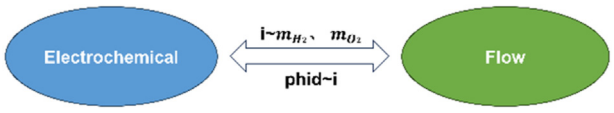

Fig. 3. Electrochemical and flow multi-physics field coupling relationships.

potential of the oxygen side is considered to be constant to the electrolytic cell voltage (E).

The flow boundary conditions use velocity inlets and pressure outlets. At the inlet boundary, the electrolyte flows at 0.22 m/s and the gas phases have no flow. All external boundaries have no-slip boundary conditions.

At the inlet boundary, the gas phase volume fraction is zero. The gas-liquid phase flows out of the outlet boundary.

3.4. Mesh independency test

The entire geometric model is assembled using a combine, where the adjacent domain boundaries share the same mesh and boundary conditions. Mesh types are divided into structured and unstructured meshes. As shown in Fig. 4(a and b), the diaphragm domain, inlet and outlet are divided into structured hexahedral mesh due to regular geometry, significantly reducing the number of meshes. Channel region due to the spherical convex-concave surface structure, can only be divided by unstructured free tetrahedral meshes.

The independence of the mesh is verified, and the differences between the calculated results of O_2 current density and average flow velocities in the Meshes 1, 2, 3 and 4, are 0.02%, 0.31%, 0.32% and 2.05%, respectively, as shown in Table 2, and the calculated results no longer change with the change of the number of meshes. Therefore, considering the calculation accuracy and calculation quantity, the Mesh 3 was selected for the numerical simulation calculation.

3.5. Solving method

Firstly, the study step is initialized using the current density distribution to obtain good initial values which are used to improve the convergence of the model. Next, the solution is solved using a steady-state solver with fully coupled calculations, using an iterative approach step by step rather than through a single computationally intensive step with a relative tolerance of less than 10^{-4}.

Table 2. Mesh-independence validation calculations.

Mesh type	Mesh 1	Mesh 2	Mesh 3	Mesh 4
Number of domain cell	14,100	29,466	102,702	926,090
Average cell mass	0.47	0.65	0.68	0.65
O2 current density	2449.5	2457.5	2459.8	2460.3
O2 Relative rate of change	0.44%	0.11%	0.02%	Baseline
Average flow velocity	0.00882	0.00900	0.00904	0.00922
Relative change rate	4.39%	2.39%	2.05%	Baseline

3.6. Model verification

The reliability of the model is verified by comparing with the voltage-current density curves of large electrolyzer operation in the Guo et al. literature [45], which is an important indicator for evaluating the performance of an electrolyzer, and the model parameters are shown in Table 3.

Figure 5(a) shows the current status of alkaline electrolyzer energy consumption up to 2018, from which it can be seen that the electrolytic cell voltage is between 1.6 V and 2.2 V under real working conditions. The comparison graph of this work with the experimental data in the literature [45] through the model results is shown in Fig. 5(b).

Table 3. Physical field parameters [32,45,52].

Physical Field Parameter	Unit	Value
Electrolyte concentration	mol/L	6.72
Electrolyte conductivity	S/m	138
H_2 side exchange current density	A/m^2	23.4
O_2 side exchange current density	A/m^2	9.3
Exchange current density (α_a, α_c)	/	0.5
Electrolytic cell voltage	V	2
Diaphragm conductivity	S/m	20.44
Electrolyte inlet flow velocity	m/s	0.22
Electrolyzer pressure	MPa	2
Operating temperature	°C	90

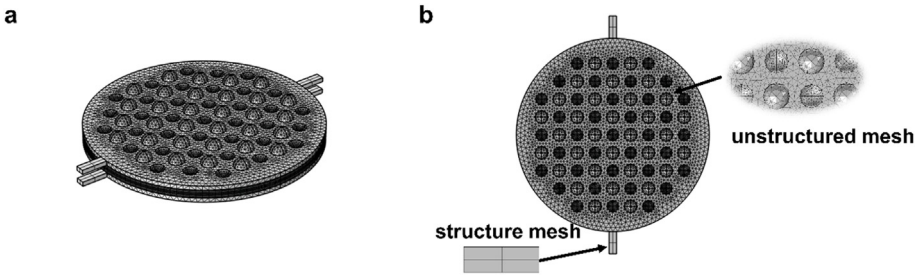

Fig. 4. Mesh delineation of filter press electrolyzer with concave-convex structure: (a) main view and (b) top view.

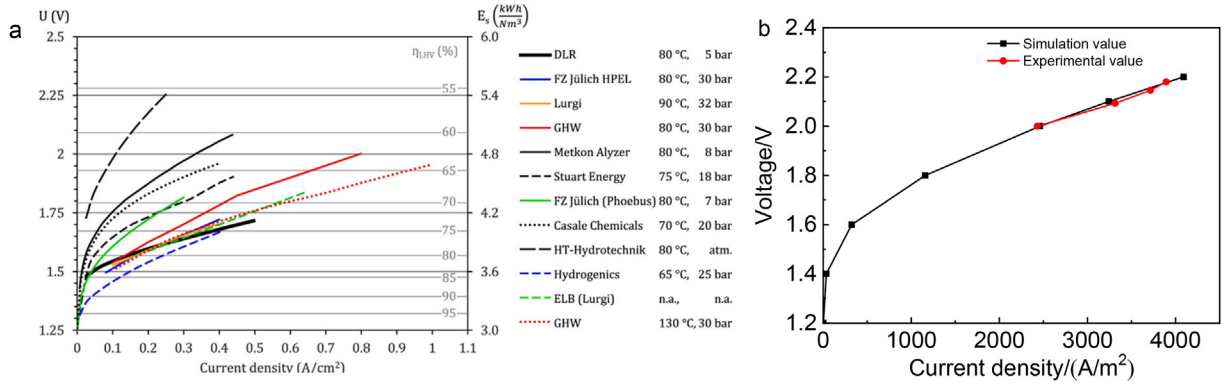

Fig. 5. (a) Typical polarization curves; (b) Comparison of the simulated (black line) and experimental values (red line) of current density-voltage polarization curves for alkaline water electrolyzer [45,53].

From the graph, it can be seen that the *I-V* curve calculated by the above simulation model in this work has the same trend with the experimental result reported in the literature, and the error is within the acceptable range, thus the numerical simulation method in this work is considered to be effective and capable of judging correctly the electrochemical performance and the electrolyte flow distribution within the electrolytic cell.

4. Results and discussion

4.1. Electrolytic cell performance

4.1.1. Electrochemical performance

Figure 6(a and b) shows the current density distribution of the electrolyte in the electrolytic cell at $Q = 0.6$ m^3/h and $E = 2.0$ V. It can be seen that, the closer to the separator center (Hz = 0.35 mm), the higher the current density of the electrolyte, with the maximum value of the current density up to 3050 A/m^2; while the closer to the bipolar plate flow channel interface (Hz = 2.7 mm), the lower the current density of the electrolyte. In addition, a significant decrease in current density in the electrode and diaphragm domains is clearly seen, with a very small current density gradient and a small voltage drop in the channel domain.

Figure 7(a and b) shows the current density distribution on the electrode within the electrolytic cell, and the trend in current density distribution of the electrolyte is opposite to that of Fig. 6, the closer to the bipolar plate (Hz = 2.7 mm), the higher the current density on the electrode surface, while the closer to the diaphragm (Hz = 0.7 mm), the lower the current density on the electrode, which is due to the co-existence of both electronic and ionic conduction within the electrolytic cell, and when close to the diaphragm, the ionic conduction is dominant, the closer to the bipolar plate channel interface, the electronic conduction is dominant, the electrolyte current is converted into

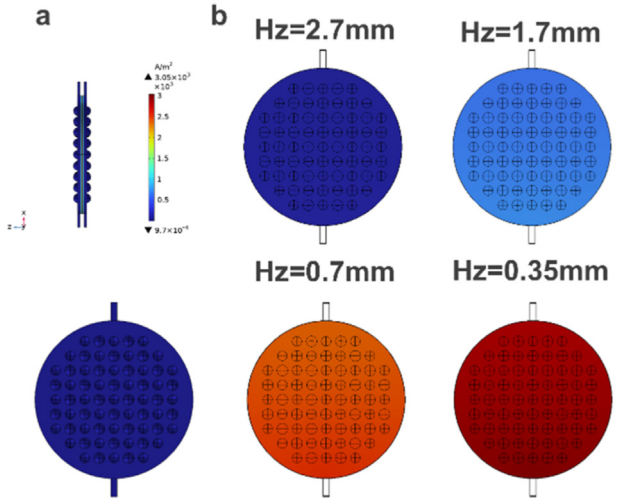

Fig. 6. (a) Side view and main view of the current density distribution of the electrolyte inside the electrolytic cell; (b) Main view of the current density distribution of the electrolyte at different heights.

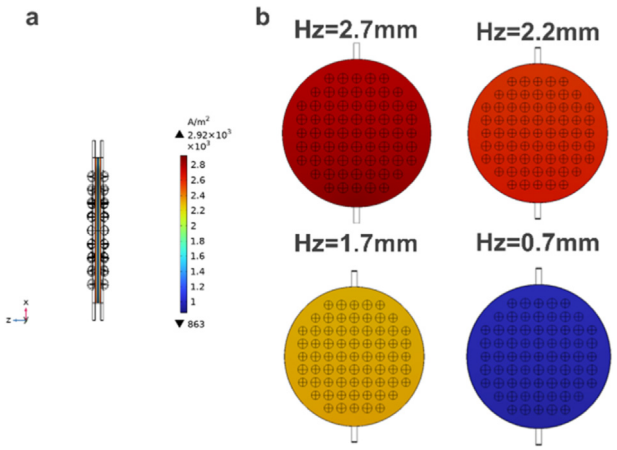

Fig. 7. (a) Side view of the current density distribution on the electrodes inside the electrolytic cell (b) Main view of the current density distribution on the electrodes at different height interfaces.

electrode current, and the current density of electrolyte decreases. Therefore, the interface where the bipolar plate is in contact with the electrode (Hz = 2.7 mm) has the highest current density on the electrode.

As can be seen from Fig. 8, the electrode current density gradually decreases along the x-direction of the outlet, considering the reason is that the bubbles are affected by buoyancy and gather towards the outlet, resulting in the closer the outlet, the electrode active specific surface area decreases and the bubble resistance increases.

From Fig. 9(a), it can be seen that the electrolyte current density near the inlet is maximum, showing a decreasing trend along the outflow x-direction. Combined with Fig. 9(b), it can be seen that the concave sphere close to the inlet has the highest current density at the edge, which is considered to be due to the increase in the flow cross-sectional area of the electrolyte when it enters the concave sphere, resulting in a decrease in the flow velocity and a decrease in the current density. At the bottom of the convex sphere in contact with the electrode, the flow cross-sectional area decreases and the flow velocity increases, and the current density is the maximum. Along the outlet x-direction, the current density inside the convex spheres decreases accordingly, and it is considered possibly that the part of the convex spheres in contact with the electrodes is also affected by the bubbles, which leads to a decrease in the current density.

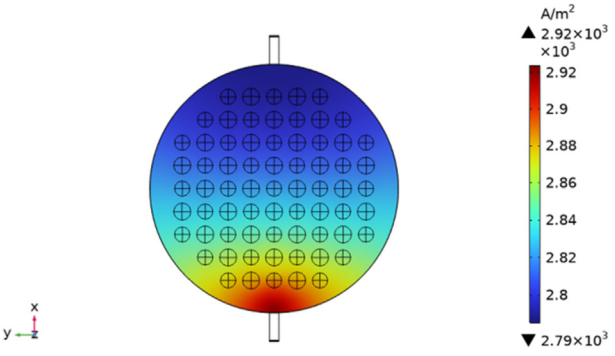

Fig. 8. Main view of electrode current density at Hz = 2.7 mm (electrode-bipolar plate contact interface).

4.2. Flow distribution

The electrolyte flow velocity distribution inside the electrolysis cell is shown in Fig. 10. From Fig. 10(a), (b), (c) and (d), it can be seen that the concave-convex structure of the flow channel leads to the uneven flow of the electrolyte, and on the same cross-section the flow velocity distribution is more uniform as closer to the center (x = 0 mm), which is attributed to the equal flow resistance at symmetric positions. Combined with Fig. 10(b) and (e), it can be seen that along the outlet x-direction, the flow velocity on the surface of the convex sphere tends to be decreased and then increased, and the minimum flow velocity is on the cross-section of x = −24 mm. Fig. 10(f) confirms there exists the vortices inside the concave-convex structure.

As shown in Fig. 11(a and b), the volume fraction on the H_2 side is nearly twice as large as that on the O_2 side, with the maximum volume fractions of 11.3% and 6.05%, respectively, due to the fact that the rate of H_2 generation is twice that of O_2. As the bubbles are influenced by buoyancy and thrust, they are continuously aggregated upwards. The non-uniformity of bubble distribution originates from the non-uniform distribution of electrolyte flow, which leads to the uneven distribution of current density, accordingly, increased the local resistance, reduced the active reaction area, increased the voltage, and limited the electrochemical reaction.

4.3. Effect of bipolar plate flow field structures

In the electrolytic cell of the concave-convex structured bipolar plate, the electrolyte flow is unevenly distributed. Moreover, the industrial

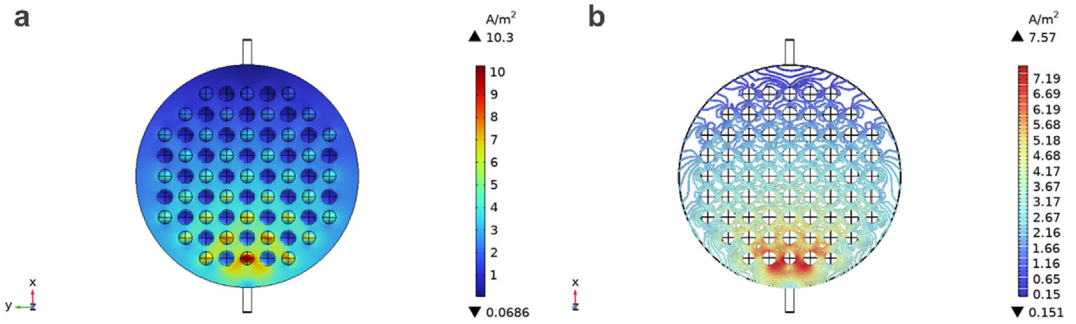

Fig. 9. (a) Electrolyte current density distribution in bipolar plate concave-convex channel field; (b) Electrolyte current density contour plot.

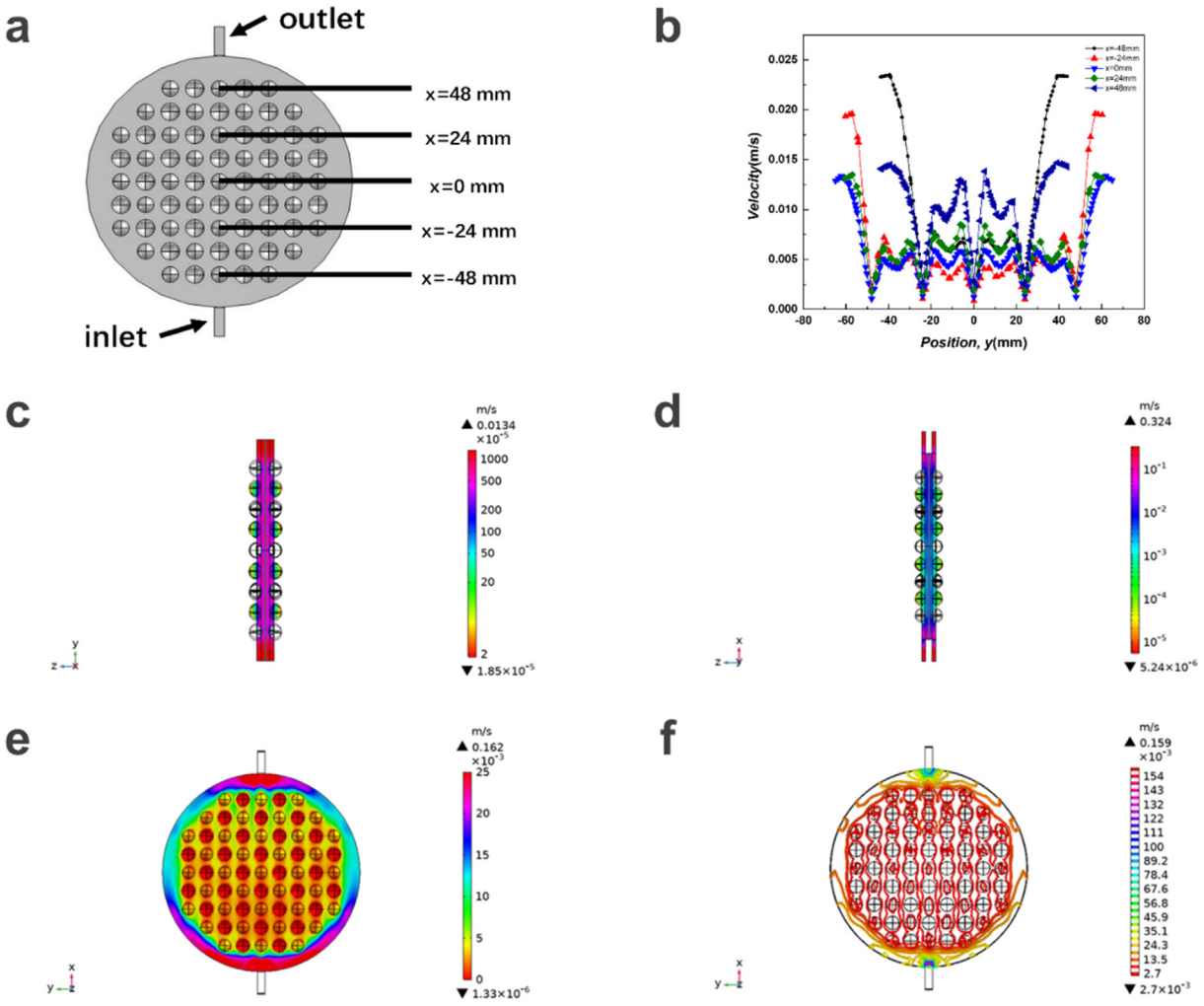

Fig. 10. (a) Locations of the transversal line for study (x-y plane, z = 2.7 mm); (b) Velocity profile on the transversal line at different y positions on the reference x-y plane (z = 2.7 mm); (c) x = 0 section flow velocity map; (d) y = 0 section flow velocity map; (e) Electrolyte flow velocity distribution inside the electrolytic cell; (f) Flow velocity contours.

concave-convex structure bipolar plates are shaped by mold punching with high processing accuracy and cost. Therefore, it is proposed to simulate and compare the bipolar plate electrolytic cells with rhombus, wedge and expanded mesh structures to study the internal electric field and flow velocity distribution of the four bipolar plate channel structures, with the same computational model, boundary conditions and mesh selection as above. The current density-voltage polarization curves for the concave-convex, rhombus, wedge and expanded mesh are shown in Fig. 12, from which it can be seen that the bipolar plate channel structure with the expanded mesh has the lowest voltage and the lowest power, and significantly higher electrochemical performance than the

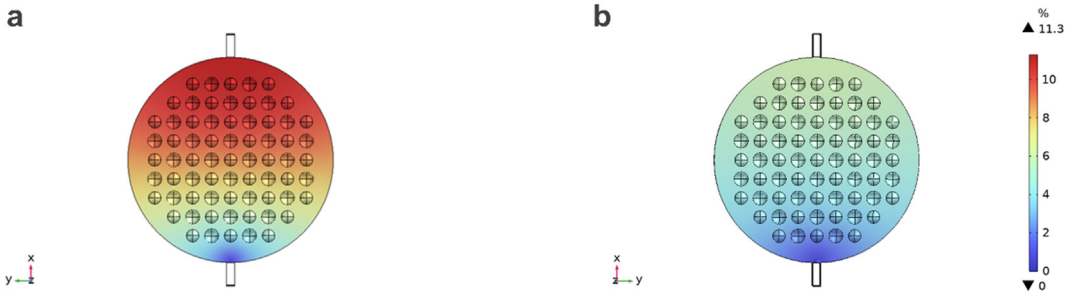

Fig. 11. (a) H_2 distribution in cathode flow path and (b) O_2 distribution in anode flow path.

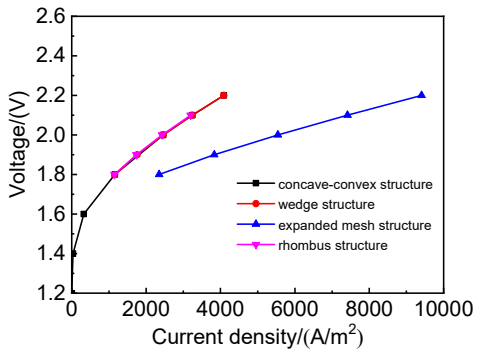

Fig. 12. Four types of channel structure I-V curves.

remaining three structures at the same current density.

As can be seen in Fig. 13(a−d), the expanded mesh structure has the greatest current density. The reason is that as described above, the current conduction is divided into electron conduction and ion conduction. With the increase of contact sites between the expanded mesh and the electrode, the enhancement of electron conduction leads to a significant increase in current density. Besides, the other three structures show a large current density at the inlet, decreasing along the x outlet direction, while along the x-exit direction, the current densities are significantly reduced due to the effect of bubble blocking.

From Fig. 14(a−e), it can be seen that the flow velocity distribution of the four bipolar plate channel structures is ranked as follows: expanded mesh structure > wedge structure > rhombus structure > concave-convex structure. Expanded mesh structure is the most uniform bipolar plate channel structure among the four structures, with a maximum flow velocity of 0.507 m/s, which not only enhances the lateral flow of electrolyte and improves the flow uniformity in the x-direction, but also greatly alleviates the existence of low-speed tailing area of wedge structure through the staggered structure, which improves the uniformity of flow velocity in the y-direction, and ultimately improves the overall flow uniformity significantly.

5. Conclusions

In this article, the electrochemical performance and electrolyte flow velocity distribution of electrolytic cell with four different bipolar plate channel structures, namely, concave-convex, rhombus, wedge and expanded mesh, are simulated, and the following conclusions can be made:

In the electrolysis cell of the concave-convex structure, the flow velocity on the surface of the convex sphere decreases and then increases along the x-direction of the outlet, with a minimum flow velocity on the cross-section of $x = -24$ mm. The presence of vortices in the flow channel domain of the concave-convex structured electrolytic cells has also been confirmed.

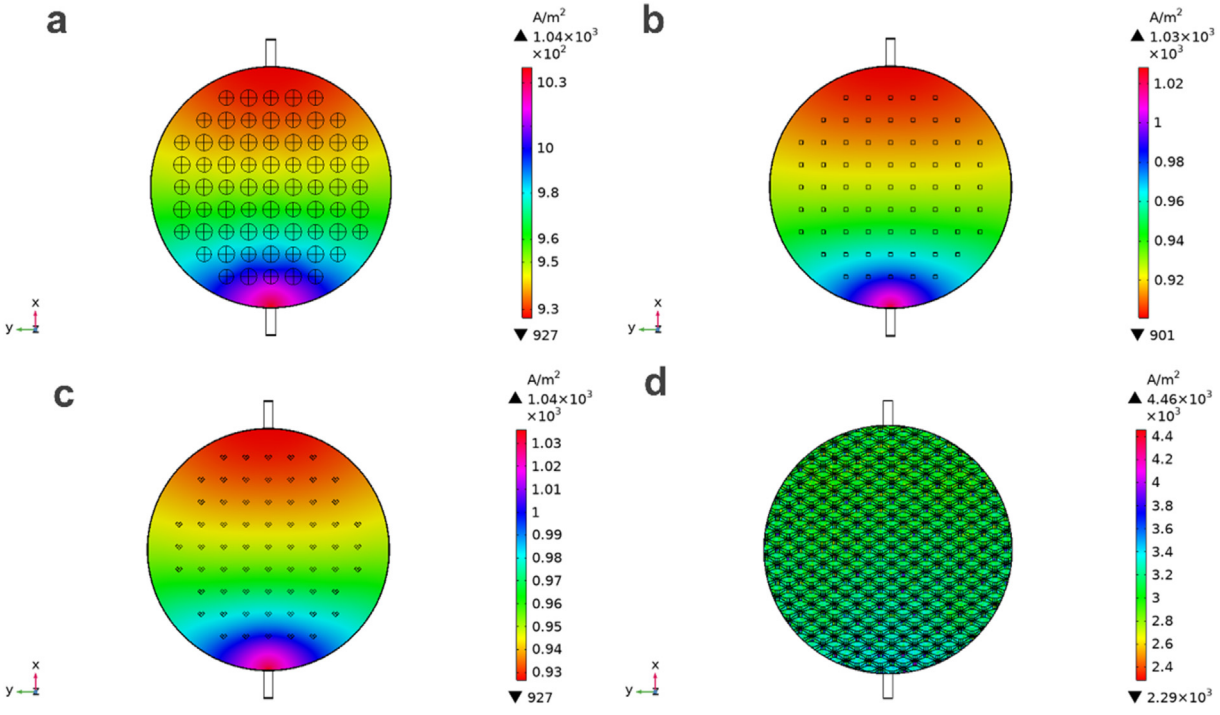

Fig. 13. Current density distributions with (a) concave-convex structure, (b) rhombus structure, (c) wedge structure and (d) expanded mesh structure.

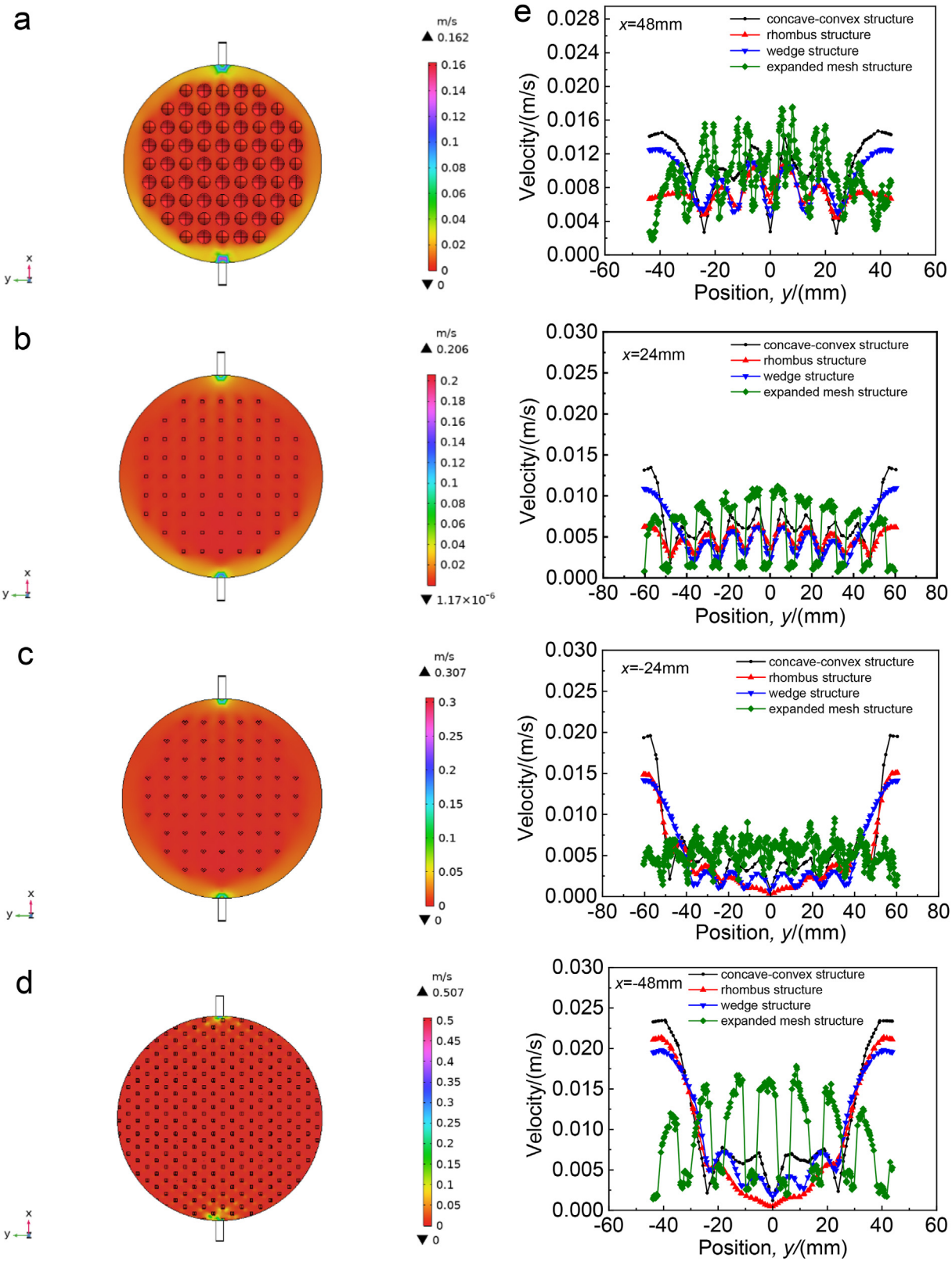

Fig. 14. Electrolyte flow velocity distributions of (a) concave-convex structure electrolyte flow velocity distribution, (b) rhombus structure electrolyte flow velocity distribution (c) wedge structure electrolyte flow velocity distribution and (d) expanded mesh structure electrolyte flow velocity distribution; (e) Velocity profile on the transversal line at different y positions on the reference x-y plane (z = 2.7 mm).

The current density-voltage polarization curves of four bipolar plate structures, namely, concave-convex, rhombus, wedge and expanded mesh, are compared, and the results indicate that at the same current density, the expanded mesh structure exhibits the lowest voltage and the lowest energy consumption. Expanded mesh structure is the most uniform bipolar plate channel structure among the above four structures, with a maximum flow velocity of 0.507 m/s.

This work provides useful guidance for the optimization design of electrolytic cell structure. In the future research, the selection of expanded mesh structure and local structure optimization will be carried out to improve the performance of the electrolytic cell, supplemented by experimental observation and verification.

Conflict of interest

The authors decline no competing interest.

Acknowledgements

This work was financially supported by the National Natural Science Foundation of China (No. 52074130) and the Engineering Research Center of Resource Utilization of Carbon-containing Waste with Carbon Neutrality, Ministry of Education.

References

[1] Chu S, Majumdar A. Opportunities and challenges for a sustainable energy future[J]. Nature, 2012, 488(7411): 294−303.
[2] Yang X, Nielsen C P, Song S, McElroy M B. Breaking the hard-to-abate bottleneck in China's path to carbon neutrality with clean hydrogen[J]. Nat. Energy, 2022, 7(10): 955−965.
[3] Sachs J D, Schmidt-Traub G, Mazzucato M, Messner D, Nakicenovic N, Rockström J. Six transformations to achieve the sustainable development goals[J]. Nat. Sustain, 2019, 2(9): 805−814.
[4] Li Y B, Hu W K, Zhang F, Li Y. Collaborative operational model for shared hydrogen energy storage and park cluster: a multiple values assessment[J]. J. Energy Storage, 2024, 82: 110507.
[5] Li J C, Xiao Y, Lu S Q. Optimal configuration of multi microgrid electric hydrogen hybrid energy storage capacity based on distributed robustness[J]. J. Energy Storage, 2024, 76: 109762.
[6] Qazi U Y. Future of hydrogen as an alternative fuel for next-generation industrial applications; challenges and expected opportunities[J]. Energies, 2022, 15(13): 4741.
[7] Prewitz M, Bardenhagen A, Beck R. Hydrogen as the fuel of the future in aircrafts − challenges and opportunities[J]. Int. J. Hydrogen Energy, 2020, 45(46): 25378−25385.
[8] Choi W, Kang S. Greenhouse gas reduction and economic cost of technologies using green hydrogen in the steel industry[J]. J. Environ. Manag., 2023, 335: 117569.
[9] Ibrahim H, Ilinca A, Perron J. Energy storage systems—characteristics and comparisons[J]. Renew. Sust. Energy Rev., 2008, 12(5): 1221−1250.
[10] Aneke M, Wang M. Energy storage technologies and real life applications − a state of the art review[J]. Appl. Energy, 2016, 179: 350−377.
[11] Yu Z Y, Duan Y, Feng X Y, Yu X, Gao M R, Yu S H. Clean and affordable hydrogen fuel from alkaline water splitting: past, recent progress, and future prospects[J]. Adv. Mater., 2021, 33(31): e2007100.
[12] Suleman F, Dincer I, Agelin-Chaab M. Environmental impact assessment and comparison of some hydrogen production options[J]. Int. J. Hydrogen Energy, 2015, 40(21): 6976−6987.
[13] Kalamaras C M, Efstathiou A M. Hydrogen production technologies: current state and future developments[J]. Conf Papers Energy, 2013, 2013: 690627.
[14] Acar C, Dincer I. Comparative assessment of hydrogen production methods from renewable and non-renewable sources[J]. Int. J. Hydrogen Energy, 2014, 39(1): 1−12.
[15] Huang W T, Zhang B H, Ge L J, He J, Liao W L, Ma P L. Day-ahead optimal scheduling strategy for electrolytic water to hydrogen production in zero-carbon parks type microgrid for optimal utilization of electrolyzer[J]. J. Energy Storage, 2023, 68: 107653.
[16] Liu Z M, Deng Y J, Wang P, Wang B H, Sun D L, Yu B. Study on the gas-liquid two-phase flow patterns for hydrogen production from electrolytic water[J]. Int. J. Hydrogen Energy, 2024, 60: 711−728.
[17] Shiva Kumar S, Lim H. An overview of water electrolysis technologies for green hydrogen production[J]. Energy Rep., 2022, 8: 13793−13813.
[18] Gambou F, Guilbert D, Zasadzinski M, Rafaralahy H. A comprehensive survey of alkaline electrolyzer modeling: electrical domain and specific electrolyte conductivity[J]. Energies, 2022, 15(9): 3452.
[19] Li Y Y, Deng X T, Gu J J, Zhang T, Guo B, Yang F Y, Ou Y MG. Comprehensive review and prospect of the modeling of alkaline water electrolysis system for hydrogen production[J]. Automot. Eng., 2022, 44(4): 567−582.
[20] Chandesris M, Médeau V, Guillet N, Chelghoum S, Thoby D, Fouda-Onana F. Membrane degradation in PEM water electrolyzer: numerical modeling and experimental evidence of the influence of temperature and current density[J]. Int. J. Hydrogen Energy, 2015, 40(3): 1353−1366.
[21] Siracusano S, Trocino S, Briguglio N, Pantò F, Aricò A S. Analysis of performance degradation during steady-state and load-thermal cycles of proton exchange membrane water electrolysis cells[J]. J. Power Sources, 2020, 468: 228390.
[22] Du N Y, Roy C, Peach R, Turnbull M, Thiele S, Bock C. Anion-exchange membrane water electrolyzers[J]. Chem. Rev., 2022, 122(13): 11830−11895.
[23] Emam A S, Hamdan M O, Abu-Nabah B A, Elnajjar E. Enhancing alkaline water electrolysis through innovative approaches and parametric study[J]. Int. J. Hydrogen Energy, 2024, 55: 1161−1173.
[24] Daoudi C, Bounahmidi T. Overview of alkaline water electrolysis modeling[J]. Int. J. Hydrogen Energy, 2024, 49: 646−667.
[25] Hu B, Liu M, Chen Q H, Zhou X W, Li H J, He M Z, Li Z Y, Zhang R, Huang Y D, Sherazi T A, Li N W. Porous polybenzimidazole membranes doped with KOH for alkaline water electrolysis[J]. J. Membr. Sci., 2024, 694: 122388.
[26] Zhang T, Song L J, Yang F Y, Ouyang M G. Research on oxygen purity based on industrial scale alkaline water electrolysis system with 50Nm^3 H_2/h[J]. Appl. Energy, 2024, 360: 122852.
[27] Liu Y, Amin M T, Khan F, Pistikopoulos E N. Safety analysis of proton exchange membrane water electrolysis system[J]. J. Environ. Chem. Eng., 2023, 11(5): 110772.

[28] Wei Q, Fan L X, Tu Z K. Hydrogen production in a proton exchange membrane electrolysis cell (PEMEC) with titanium meshes as flow distributors[J]. Int. J. Hydrogen Energy, 2023, 48(93): 36271−36285.
[29] de Groot M T, Kraakman J, Garcia Barros R L. Optimal operating parameters for advanced alkaline water electrolysis[J]. Int. J. Hydrogen Energy, 2022, 47(82): 34773−34783.
[30] Phillips R, Edwards A, Rome B, Jones D R, Dunnill C W. Minimising the ohmic resistance of an alkaline electrolysis cell through effective cell design[J]. Int. J. Hydrogen Energy, 2017, 42(38): 23986−23994.
[31] Zhang Y F. Study of influencing factors of cell voltage in filter-press type electrolyzer[D]. Hunan University, 2015.
[32] Li J. Simulation study on flow characteristics in the unit of filter-press water electrolyzer[D]. China University of Petroleum, 2020.
[33] Yu P, Wang F M, Shifa T A, Zhan X Y, Lou X D, Xia F, He J. Earth abundant materials beyond transition metal dichalcogenides: a focus on electrocatalyzing hydrogen evolution reaction[J]. Nano Energy, 2019, 58: 244−276.
[34] Haverkort J W, Rajaei H. Voltage losses in zero-gap alkaline water electrolysis[J]. J. Power Sources, 2021, 497: 229864.
[35] Liu L P, Wang J Y, Ren Z B, Wang F, Wang T, Guo H J. Ultrathin reinforced composite separator for alkaline water electrolysis: comprehensive performance evaluation[J]. Int. J. Hydrogen Energy, 2023, 48(62): 23885−23893.
[36] Olivier P, Bourasseau C, Bouamama P B. Low-temperature electrolysis system modelling: a review[J]. Renew. Sustain. Energy Rev., 2017, 78: 280−300.
[37] Hammoudi M, Henao C, Agbossou K, Dubé Y, Doumbia M L. New multi-physics approach for modelling and design of alkaline electrolyzers[J]. Int. J. Hydrogen Energy, 2012, 37(19): 13895−13913.
[38] Huang D J, Xiong B Y, Fang J K, Hu K W, Zhong Z Y, Ying Y H, Ai X M, Chen Z. A multiphysics model of the compactly-assembled industrial alkaline water electrolysis cell[J]. Appl. Energy, 2022, 314: 118987.
[39] Hu S, Guo B, Ding S L, Yang F Y, Dang J, Liu B, Gu J J, Ma J G, Ouyang M G. A comprehensive review of alkaline water electrolysis mathematical modeling[J]. Appl. Energy, 2022, 327: 120099.
[40] Zhang Z Z, Jin L M, Deng L A, Li W B, Liu M, Geng Z, Zhang C M. Three-dimensional simulation of two-phase flow distribution in spherical concave-convex shaped flow field for alkaline water electrolyzer[J]. Int. J. Hydrogen Energy, 2023, 48(86): 33401−33410.
[41] Wang T, Wang J Y, Wang P J, Wang F, Liu L P, Guo H J. Non-uniform liquid flow distribution in an alkaline water electrolyzer with concave-convex bipolar plate (CCBP): a numerical study[J]. Int. J. Hydrogen Energy, 2023, 48(33): 12200−12214.
[42] Wang T, Wang J Y, Wang P J, Ren Z B, Yan X P, Wang W, Guo W Q. Plate structure design guideline for commercial alkaline water electrolyzers (AWEs) with improved liquid flow uniformity: multi-scale quantitative criteria and experimental validation[J]. Int. J. Hydrogen Energy, 2023, 49: 907−924.
[43] Zhao P C, Wang J G, He W, Sun L M, Li Y. Alkaline zero gap bipolar water electrolyzer for hydrogen production with independent fluid path[J]. Energy Rep., 2023, 9: 352−360.
[44] Zhao P C, Wang J G, Sun L M, Li Y, Xia H T, He W. Optimal electrode configuration and system design of compactly-assembled industrial alkaline water electrolyzer[J]. Energy Convers. Manag., 2024, 299: 117875.
[45] Zouhri K, Lee S Y. Evaluation and optimization of the alkaline water electrolysis ohmic polarization: exergy study [J]. Int. J. Hydrogen Energy, 2016, 41(18): 7253−7263.
[46] Ding S L, Guo B, Hu S, Gu J J, Yang F Y, Li Y Y, Dang J, Liu B, Ma J G. Analysis of the effect of characteristic parameters and operating conditions on exergy efficiency of alkaline water electrolyzer[J]. J. Power Sources, 2022, 537: 231532.
[47] Cha Q X. Introduction to the dynamics of electrode processes[M]. Bejing: Science Press, 2002.
[48] Guo Y J. Structural design and performance optimization of an alkaline water hydrogen electrolyzer[D]. Beijing University of Chemical Technology, 2020.
[49] Le Bideau D, Mandin P, Benbouzid M, Kim M, Sellier M, Ganci F, Inguanta R. Eulerian two-fluid model of alkaline water electrolysis for hydrogen production[J]. Energies, 2020, 13(13): 3394.
[50] Cao X P, Zhao N, Zhang S R, Zhou L L, Hu Y Q, Yun J. Investigation of the hydrogen bubble effect on the overpotential in an alkaline water electrolyzer[J]. Int. J. Hydrogen Energy, 2024, 49: 47−57.
[51] Li D. Principles of electrochemistry[M]. Beijing: Beijing University of Aeronautics and Astronautics Press, 2008.
[52] Gao L Y, Yang L, Wang C H, Dan G X, Huo X Y, Zhang M F, Li W, Zhang J L. Three-dimensional two-phase CFD simulation of alkaline electrolyzers[J]. J. Electrochem., 2023, 29(9): 25−40.
[53] Buttler A, Spliethoff H. Current status of water electrolysis for energy storage, grid balancing and sector coupling via power-to-gas and power-to-liquids: a review[J]. Renew. Sustain. Energy Rev., 2018, 82: 2440−2454.

利用膨胀网作为双极板流道结构优化碱性水电解槽

熊海燕[a]，朱振啸[a]，高　鑫[a]，范晨铭[a]，栾辉宝[b,*]，李　冰[a,*]
[a]华东理工大学，上海 200237
[b]中国船舶有限公司第七一一研究所，上海 201108

摘要

碱性水电解制氢是现今最为成熟的水电解制氢技术。电解槽由多个电解小室组成，单个电解小室由隔膜、电极、双极板和端板等组成。现有工业的双极板流道结构为凹凸结构，通过模具冲压成型制备，制备成本高且困难。凹凸结构电解小室存在电解液流动不均匀和电流密度低的问题，进而增加了碱性水电解制氢的能耗和成本。因而，本文首先根据现有工业的凹凸双极板流道结构搭建电化学和流动模型，分析电解小室电流密度、电解液流动和气泡分布情况。模型可靠性已通过与文献实验数据对照验证。其中，电化学电流密度决定了气体产率，气体在电解液中流动反过来影响电化学反应活性比表面积和欧姆电阻。结果表明，凹凸结构电解小室凹球底部流动速度几近为零，凸球表面电解液流速较大，流道结构中存在旋涡，电解液分布不均。接着，建模优化碱性水电解槽的流道结构，比较了凹凸结构、网状、菱形和膨胀网结构电解小室电化学和流动性能。结果表明，膨胀网结构电解小室电流密度最大，为 3330 A/m^2，电解液流速最大，为 0.507 m/s。相同电流密度下，过电位最小，能耗最低。本文对碱性水电解槽流道结构的全面理解和优化提供一定的指导意义，为大规模电解槽设计提供理论基础。

关键字：碱性水电解槽；膨胀网流道结构；数值模拟